Journal Pre-proofs

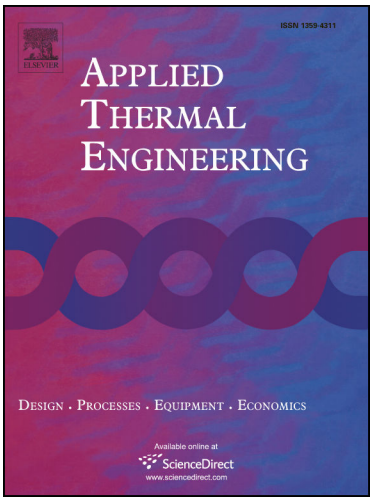

An X-lattice cored rectangular honeycomb with enhanced convective heat transfer performance

Hongbin Yan, Qiancheng Zhang, Weijian Chen, Gongnan Xie, Jianjun Dang, Tianjian Lu

PII: S1359-4311(19)35237-8
DOI: https://doi.org/10.1016/j.applthermaleng.2019.114687
Reference: ATE 114687

To appear in: *Applied Thermal Engineering*

Received Date: 30 July 2019
Revised Date: 11 November 2019
Accepted Date: 15 November 2019

Please cite this article as: H. Yan, Q. Zhang, W. Chen, G. Xie, J. Dang, T. Lu, An X-lattice cored rectangular honeycomb with enhanced convective heat transfer performance, *Applied Thermal Engineering* (2019), doi: https://doi.org/10.1016/j.applthermaleng.2019.114687

An X-lattice cored rectangular honeycomb with enhanced convective heat transfer performance

Hongbin Yan [a], Qiancheng Zhang [b], Weijian Chen [c], Gongnan Xie [a], Jianjun Dang [a, *], Tianjian Lu [b, d, *]

[a] *School of Marine Science and Technology, Northwestern Polytechnical University, Xi'an 710072, PR China*

[b] *State Key Laboratory for Strength and Vibration of Mechanical Structures, Xi'an Jiaotong University, Xi'an 710049, PR China*

[c] *Key Laboratory of Aircraft Environment Control and Life Support, Ministry of Industry and Information Technology, Nanjing University of Aeronautics & Astronautics, Nanjing 210016, PR China*

[d] *State Key Laboratory of Mechanics and Control of Mechanical Structures, Nanjing University of Aeronautics and Astronautics, Nanjing 210016, PR China*

* Corresponding authors: tjlu@nuaa.edu.cn (Tianjian Lu); janjund@nwpu.edu.cn (Jianjun Dang).

ABSTRACT

This paper proposes a new periodic cellular material (PCM) by integrating the X-lattice into a rectangular honeycomb. Convective heat transfer in this new PCM is explored. For a given Reynolds number, the overall Nusselt number of the new PCM is up to 360% and 55% higher than the parent honeycomb and X-lattice sandwich panel, respectively. The introduction of the honeycomb walls to the X-lattice sandwich panel enlarges or induces new separation vortices near the four corners of each rectangular passage, which weakens the tangential flow perpendicular to the mainstream; the no-slip honeycomb walls and the modification of the separation vortices change the counter-rotating vortex pair behind the ligaments, significantly reduce the bulk turbulent kinetic energy magnitude and limit the convective transport of the high turbulent kinetic energy to the endwalls, due to severe dissipation of the energy by the viscous sub-layer. Corresponding to the flow pattern variations, local heat transfer on the endwall and the X-lattice ligaments is deteriorated. However, the X-lattice induced spiral flow and secondary flows enhance the heat transfer on the honeycomb walls by approximately 230%. For a given pumping power, the new PCM exhibits up to 42% higher heat removal than the parent X-lattice sandwich.

KEYWORDS: Periodic cellular material; X-lattice; Rectangular honeycomb; Turbulent heat transfer enhancement; Thermo-fluidic mechanisms

NOMENCLATURE

b_1, b_2	the widths of the intersection point of two ligaments as shown in Fig. 3(b) (m)
c_p	the specific heat of air (J/(kgK))
C_p	dimensionless pressure coefficient as defined in Eq. (9)
f_H	dimensionless friction factor based on the lattice core height as defined in Eq. (6)
h_i	the overall heat transfer coefficient corresponding to the i^{th} unit cell as defined in Eq. (4) (W/(m^{2}K))
H_c	the height of the periodic cellular cores (m)
i	the serial number of the X-lattice unit cells
k_e	specific turbulent kinetic energy (J/kg)
k_f, k_s	the thermal conductivities of air and the solid material, respectively (W/(mK))
l	the length of an X-lattice unit cell (m)
L	the length of the test sample (m)
Nu	local Nusselt number based on lattice core height
Nu_{ave}	area-averaged value of local Nusselt number
Nu_H	average overall Nusselt number as defined in Eq. (3)
Nu_i	overall Nusselt number corresponding to the i^{th} unit cell as defined in Eq. (3)
p	local static pressure at an arbitrary position (Pa)
p_{min}	the minimum pressure on a specific x-y plane (Pa)
Pr	the Prandtl number of air
q''	heat flux (W/m^2)
r_1 • r_4	radii of the fillets as shown in Fig. 3(b) (m)
Re_H	Reynolds number as defined in Eq. (2)
t_f	the thickness of the honeycomb walls perpendicular to the endwalls (m)
t_l	the thickness of the X-lattice ligaments (m)
t_s	the thickness of the substrates (m)
$T_{f,i}$	bulk mean fluid temperature corresponding to the i^{th} unit cell as defined in Eq. (5) (ëC)

T_i the measured wall temperature corresponding to the i^{th} unit cell (°C)

T_{in} the air temperature at the inlet of the test section (°C)

U_c centerline velocity measured upstream the test sample (m/s)

U_{mc} mean velocity overall channel height (m/s)

V_m velocity magnitude (m/s)

V_t tangential velocity magnitude (m/s)

w the width of a half X-lattice unit cell (m)

w_j the width of the joint between the endwall and the lattice ligaments as shown in Fig. 3(b) (m)

w_l the width of an X-lattice ligament as shown in Fig. 3(b) (m)

W the width of the test sample as shown in Fig. 3(a) (m)

x, y, z the three components of an Cartesian coordinate system (m)

y^+ the dimensionless wall distance

Greek symbols

•, •• the included angles between the lattice ligaments as shown in Fig. 3(b) (°)

• Δp the pressure drop through the sample under investigation (Pa)

•• the dynamic viscosity of air (Pa·s)

•• the density of air (kg/m^3)

Abbreviations

OA orientation A of the X-lattice as shown in Fig. 1

OB orientation B of the X-lattice as shown in Fig. 1

PCMs periodic cellular materials

SCMs stochastic cellular materials

WBK wire-woven bulk Kagome

1. INTRODUCTION

Open-cell cellular metals with high porosity and specific surface area topologies are promising multifunctional materials for engineering applications where the material is required to have multiple functions such as simultaneous mechanical load bearing and convective heat/mass transfer [1]. Typical examples include active thermal protection of aerospace vehicles [2], active cooling of jet blast deflectors on an aircraft carrier

[3], passive cooling of ventilated brake discs for high-performance vehicles [4] as well as catalyst supporting for automobiles [5]. Based on the topology, they can be classified into stochastic cellular materials (SCMs) such as metal foams [6] and periodic cellular materials (PCMs) as those schematically shown in Fig. 1 [1, 7-13]. In general, PCMs are mechanically superior to SCMs for a given porosity because their deformation is dominated by cell wall stretching/compression in contrast to cell wall bending for SCMs [1]. Therefore, PCMs may be more suitable when mechanical strength is a necessity.

As outputs of efforts during the past decades, PCMs with a variety of topologies as those shown in Fig. 1 have been invented and fabricated by using various manufacturing technologies. The metal sheet assembling and brazing method can be used to fabricate simple two-dimensional PCMs such as square honeycombs [7]. By using the weaving and brazing method, complex textiles with several topologies can be fabricated with metal wires, such as the diamond/square woven textile [14] and wire-woven bulk Kagome (WBK) [5]. With the investment casting method, the tetrahedral, pyramidal and Kagome lattices without sharp edges on the ligaments can be fabricated [1]. In addition, the metal sheet folding method can be used to make the tetrahedral [12], pyramidal and X-type lattices [13] with sharp-edged ligaments. Recently, additive manufacturing technology is adopted to fabricate more complex PCMs [15]. At present, folding expanded metal sheet with specifically designed patterns [16] is easier to implement with production lines and more cost-effective compared to other methods. Although the additive manufacturing allows more flexible design of the cell topology, its widespread application depends on drastic suppression of cost in the future.

As expected, the topologies of the above PCMs have great effect on their thermo-fluidic properties. For the two-dimensional PCMs, Wen et al. [7] presented a comprehensive study of convective heat transfer in square, diamond, trapezoidal and hexagonal honeycombs; they found that both heat transfer and pressure drop increases with increasing surface area density and the shape factor; for a given Reynolds number or coolant flow rate, however, the straight channel endows the honeycombs with evidently lower heat transfer coefficient relative to other PCMs, although the pressure drop is lower.

For the three-dimensional PCMs, Kim et al. [10, 17-19] conducted detailed analysis of both the overall and detailed flow and heat transfer characteristics in tetrahedral lattice sandwich panels with casted circular ligaments; they found that the heat removal from the ligaments is similar to that of banks of cylinders; in addition, the formation of horse shoe vortex significantly enhances heat transfer on the endwall. Similar studies were carried out by Gao et al. [20] on a composite tetrahedral lattice sandwich panel. Zhang et al. [21]

numerically compared the thermal performance between two tetrahedral lattice sandwich panels separately fabricated by casting and metal sheet folding; for a given porosity and Reynolds number, they found that the folded lattice with shape-edged rectangular cross-sectioned ligaments results in higher heat transfer and pressure drop relative to the casted lattice with circular ligaments; for a given pumping power, the cheaper folded lattice have similar thermal performance to the expensive casted one, highlighting its superiority in terms of engineering applications. For the Kagome PCMs, Hoffmann et al. [11] investigated the convective heat transfer in a casted Kagome lattice sandwich panel; they found that the flow orientation relative to the core has evident effect on the pressure drop and heat transfer; pressure drop and heat transfer increases with the increase of core porosity. Joo et al. [9, 22] and Feng et al. [3] investigated the forced convective heat transfer in multi-layered WBK sandwich panels; they found that the brazing of the helical wires at their intersection section can evidently enhance the heat transfer but have negligible effect on pressure drop; they also made a comparison between their WBK and a single-layered Kagome fabricated by casting in [11] and found that the WBK is superior. Given that the comparisons in [3, 9, 22] may be unfair because the WBK and Kagome sandwich panels have evidently different dimensions and number of layers of the unit cells along sandwich height, Shen et al. [23] made a more reasonable comparison between a single layered WBK and a single layered Kagome with exactly the same porosity and overall dimensions; for a given Reynolds number, they found that the heat transfer of the Kagome lattice is actually superior than that of the WBK lattice, while the pressure drop is similar. Based on the comparisons above and those by Yang et al. [24] and Bai et al. [25], the Kagome PCM seems to be thermally superior than the tetrahedral PCM. Recently, Chaudhari et al. [26] and Ekade et al. [27] investigated the convective heat transfer of the octet truss lattices with different porosities and pore densities; they found that the heat transfer performance of the octet truss lattice is not inferior to the metal foams, while the pressure drop is lower. Ho et al. [15] further investigated several PCMs with different configurations of the Rhombi-Octet unit cells; they found that these PCMs exhibit lower friction factor and heat transfer coefficient than metal foams.

Yan et al. presented the convective heat transfer characteristics of a geometrically anisotropic X-lattice sandwich panel; two representative orientations, i.e., orientation A (OA) [28] and orientation B (OB) [29] as shown in Fig. 1 were selected for the investigations; for a given porosity and Reynolds number, they found that OA of the X-lattice sandwich panel exhibited up to 170% higher heat transfer than the Kagome and tetrahedral lattices [28]; for a given pumping power, the thermal performance of both orientations is superior

to the reference Kagome and tetrahedral lattices [28, 29]; further exploration shows that the unique topology of the X-lattice in OA induces large scale spiral primary flow and three kinds of secondary flows as indicated by the streamlines in Fig. 2(a), which were argued to be responsible for its improved thermal performance [28]. A similar study by Jin et al. [30] further reveals that the heat transfer of the X-lattice is much better than that of the pyramidal lattice under both the fixed Reynolds number and pumping power conditions. In view of the above, the cost effective X-lattice fabricated by folding expanded metal sheet may compete with most of the multifunctional heat dissipation media reported in the open literature.

Motivated by the unique primary and secondary flows as shown in Fig. 2(a) for OA of the X-lattice, this paper introduces a new PCM called "X-lattice cored rectangular honeycomb" as shown in Fig. 2(b). In each passage of the honeycomb, an array of half X-lattice unit cells is inserted and connected to the honeycomb walls. With this modification, three aspects of improvements are expected. First, local heat transfer on the honeycomb walls may be substantially enhanced by the strong spiral flow and vortex induced turublence on the symetrical plane as shown in Fig. 2(a). Second, compared with a bare X-lattice, the introduction of the honeycomb wall to the X-lattice can further restrict the freedom of the intersection point of the ligaments, which can further improve the mechanical strength of the X-lattice according to [31]. Finally, the introduction of the honeycomb separates the X-lattice into separated passanges, which is important to supress fluid maldistrubition in applications of the X-lattice in thermal management systems, heat exchangers, etc.

Hence, this paper presents a comprehensive study of the forced convective fluid flow and heat tranfer in the new PCM by comparing it with the parent rectangular honeycomb and the X-lattice. To this end, a series of experiments and numerical simulations were conducted. Main focuses of this paper are: (a) how the honeycomb walls modify local heat tranfer on the X-lattice surface; (b) how the X-lattice modifies local heat transfer on the honeycomb walls; (c) the fluidic mechanisms underlying the above effects.

2. EXPERIMENTAL DETAILS

Although a detailed validation of the numerical models for bare X-lattice sandwich panels has been performed by comparison between experimental and numerical results [28, 29], further validating the numerical model for the present X-lattice cored honeycomb is still necessary since the introduction of the honeycomb walls adds additional confinement to the flow through the X-lattice unit cells. To this end, a new sample was fabricated and tested by modifying the test section of the experimental system previously presented

in [29].

2.1. Test sample and facilities

A photograph of the single-layered X-lattice cored honeycomb is shown in Fig. 3(a). It was fabricated by three-dimensional printing with Inconel 718 stainless steel having a thermal conductivity of ~11.4 W/(mK) [32]. To fabricate the test sample, geometric model of the test sample should be obtained first. To this end, geometrical model of the X-lattice with exactly the same morphology as that in [28, 29] was constructed by using the sheet metal tools in the commercial software package Solidworks™ 2013; then two substrates tangential to the lattice core were modeled; afterwards, two fillets with the radius of 1.0 mm were built between each node of the lattice and the substrate; finally, the sharp edges of the fillets were removed to eliminate defections during printing. More details of the geometric model have been presented in [28, 29]. The model was imported into the machine to print the test sample.

The test sample incorporates 18 passages in the transverse direction (i.e., the *x*-direction as shown in Fig. 3(a)) and 10 X-lattice unit cells along the *z*-direction to minimize the sidewall, entry and exit effects according to previous studies [28, 29]. The corresponding width (W) and length (L) of the sample are 127 mm and 120 mm, respectively. Detailed parameters of the unit cell of the X-lattice cored honeycomb are schematically illustrated in Fig. 3(b) with the aid of isometric view and front views separately in OA and OB. The values of the parameters are summarized in Table 1.

The open-loop wind tunnel system for heat transfer and pressure drop measurements is illustrated in Fig. 4(a). It is mainly composed of the air supply and control system, the test section and the data acquisition system. Ambient air is pumped into the wind tunnel by a centrifugal blower. The air flow rate can be varied by changing the rotational speed of the blower through an inverter. To break up the large-scale vortices induced by abrupt expansion of air, a fine screen layer is installed after the inlet of the tunnel. Several hexagonal honeycombs are installed subsequently to make the flow parallel to the flow channel, followed by another mesh screen. Afterwards, the flow experiences a carefully designed two-dimensional contraction and enters the test section.

The test section is made of transparent Perspex plates. Since the height of the tunnel exit is bigger than the height of the test sample, a two-dimensional contraction and a fine honeycomb layer are introduced at the inlet of the test section. To make the flow fully developed before entering the sandwich panel and leaving the

test rig, two long flow passages with a length of ~46H_c are designed upstream and downstream the test sample. The sample is embedded into the channel with the inner endwalls flush with the inner surface of the channel walls. To eliminate flow leakage, the test section is securely sealed with a silicon sealant.

To obtain the coolant flow rate, a stagnation pressure probe is installed at the centroid of the channel cross-section placed 9H_c upstream the test sample, where a static pressure tap is also installed at the channel wall. Thus the centreline velocity (U_c) can be measured. In addition, another stagnation pressure probe mounted on a traverse table and a static pressure tap are used to measure the fully developed velocity profiles at the channel exit; therefore, the mean velocity (U_{mc}) over channel height can be obtained by integrating the velocity profile. In this way, a correlation between U_{mc} and U_c is obtained as follows:

$$U_{mc} = 0.8097U_c + 0.1426 \quad (1)$$

The determination coefficient of this correlation is 0.9993. More details can be found in [29].

2.2. Heat transfer and pressure drop measurements

For heat transfer measurement, the heating and temperature measurement assembly is carefully designed as shown in Fig. 4(b). A flexible heating pad composed of etched Inconel foils and Kapton electrical insulation films is used to heat the sample through the bottom substrate. A copper plate with a thickness of 0.5 mm is used as a thermal spreader plate to minimize the thermal non-uniformity caused by the gaps between adjacent heating foils. To measure endwall temperature, grooves with a depth of 0.5 mm were fabricated on the bottom substrate; ten bead-type thermocouples (OMEGA™ TT-T-36) with a bead diameter of 0.4 mm were embedded in the grooves; the thermocouples are located at the centreline of the flow passage with an streamwise interval of 12 mm as shown in Fig. 4(b). To minimize thermal contact resistance, a thermal glue (Artic Silver™) was used to fill the gaps in the grooves and to bond the above heating pad to the substrate. During experiments, the test section was covered by thick rubber plastic foam to minimize heat loss. To measure air temperatures, two additional thermocouples (OMEGA™ TT-T-36) are installed separately upstream the test sample and at the exit of the test section.

For pressure drop measurement, two static pressure taps are installed at the upstream side and downstream side of the test sample, respectively. The distance between each tap and the edge of the sample substrate is 6 mm. Detailed operating conditions of the present experiments are summarized in Table 2, where the Reynolds number (Re_{H_1}) is defined in the next section.

2.3. Data reduction and measurement uncertainties

To compare the present X-lattice cored honeycomb with the parent X-lattice and rectangular honeycomb, the Reynolds number (Re_H) is defined as:

$$Re_H = \frac{\rho H_c U_{mc}}{\mu}\left(1 + \frac{t_f}{w}\right) \tag{2}$$

where ρ is the density of air; H_c is the channel height; μ is the dynamic viscosity of air; t_f and w are the thickness of the honeycomb wall and the width of a half X-lattice unit cell as shown in Fig. 3, respectively. This definition is also applicable for the bare X-lattice with $t_f = 0$.

To evaluate overall heat transfer, the overall Nusselt number is used and defined as:

$$Nu_H = \sum_{i=1}^{10} Nu_i = \sum_{i=1}^{10} \frac{h_i H_c}{k_f} \tag{3}$$

where k_f is the air thermal conductivity based on the arithmetic mean temperature at the inlet and outlet of the test section. h_i is the overall heat transfer coefficient measured by the thermocouples corresponding to the i^{th} unit cell, defined as:

$$h_i = \frac{q''}{T_i - T_{f,i}} \tag{4}$$

where q'' is the heat flux imposed by the heating pad; T_i and $T_{f,i}$ is the measured wall temperature and bulk mean fluid temperature, respectively. According to the coordinate system as shown in Fig. 4, $T_{f,i}$ can be calculated based on the energy balance as:

$$T_{f,i} = T_{in} + \frac{(i - 0.5) l q''}{\rho U_{mc} H_c c_p} \tag{5}$$

where T_{in} is the inlet air temperature; i is the serial number of the unit cell; l is the length of the X-lattice unit cell as shown in Fig. 3(b); c_p is the specific heat of air.

For pressure drop evaluation, the friction factor is used and defined as:

$$f_H = \frac{\Delta p H_c}{L} \Big/ \frac{1}{2}\left(1 + \frac{t_f}{w}\right) U_{mc}^2 \tag{6}$$

where Δp is the pressure drop through the sample with a streamwise length of L.

Based on the root mean square method [33], measurement uncertainties were estimated for the present study. Pressure was recorded by a Scanivalve™ 3217 pressure transducer with a resolution of 0.3 Pa.

Temperature was measured by an Aglient™ 34970A module; the corresponding uncertainty is 0.1 °C. More details of the measurement instruments are available in [28, 29]. According to the energy balance, heat loss through the channel walls were calculated based on the heating power input as well as the inlet and outlet air temperatures; correspondingly, the actual heat flux applied to the sample was obtained by subtracting the heat loss from the power input. The variation of the air thermal conductivity was estimated to be less than 3.0%. Therefore, the uncertainties for Reynolds number, Nusselt number and friction factor are less than 1.0%, 6% and 2%, respectively.

3. NUMERICAL SIMULATION

To facilitate a comprehensive comparison among the X-lattice cored honeycomb, the bare X-lattice and the rectangular honeycomb, three-dimensional simulations were carried out by using ANSYS 15.0. After validation of the numerical model against the experimental data, detailed fluid flow and local heat transfer characteristics are analysed and compared. Details of the numerical models are presented below.

3.1. Computational domain and boundary conditions

Fig. 5(a) presents the solid and fluid domains simulated in the numerical models. Due to geometric symmetry, only one passage is considered. Relevant dimensions of the bare honeycomb and the X-lattice are the same as those of the X-lattice cored honeycomb. A short channel with a length of H_c and a longer channel with a length of $6H_c$ are included upstream and downstream the sample for better convergence of the numerical solution.

Symmetric conditions are used for the symmetric pairs of both the solid and fluid domains. For the inlet boundary, fully developed turbulent flow between two parallel plates is simulated first; then the obtained flow field and a constant fluid temperature are applied to the inlet of the domains as boundary condition. Validation of the inlet boundary condition is available in [29]. At the outlet, mass flow rate is specified according to the inlet conditions to ensure mass conservation. Constant heat flux is imposed at the outer surface of the bottom substrate. Conservative interface flux boundary conditions are used at all the solid-fluid interfaces. Other surfaces of the computational domain are set to be adiabatic. All the solid walls are set to be no-slip walls.

3.2. Numerical methods and mesh independency

As shown in Fig. 5(b), for the rectangular honeycomb, structured hexahedral elements are generated by

ANSYS ICEM CFD 15.0 to discretise the computational domains for its geometrical simplicity; for the other two structures, tetrahedral elements in conjunction with prism layers near the solid walls are used. The flows in the rectangular honeycomb, the X-lattice sandwich panel and the X-lattice cored honeycomb are thought to be turbulent according to the Reynolds number range in Table 2. Therefore, the height of the first layer of elements on the solid walls is about 0.01 mm to ensure a dimensionless wall distance (y^+) less than 1.0.The flow is assumed to be steady and incompressible. At each Reynolds number, thermo-physical properties of air upstream and downstream the tested X-lattice cored honeycomb are calculated in the NIST software [38] according to the measured air temperatures and pressures. Then the arithmetic mean values are finally used in the numerical simulations for all the PCMs, as summarized in Table 3. In addition to the Inconel 718 stainless steel, aluminium with a thermal conductivity of 236 W/(mK) is also considered to clarify the effects of material thermal conductivity on relative merits among the three PCMs.

The shear stress transport turbulent model [34, 35] is used to incorporate turbulence effect due to its good performance in predict convective heat transfer in various PCM sandwich panels [21, 23, 28-30] and smooth channels [36, 37]. The corresponding governing equations for mass, momentum, turbulent kinetic energy, turbulent frequency and energy conservations have been presented in [21, 30], which are not included here for brevity.

The high resolution scheme and the central difference scheme are used to discretise the advection and diffusion terms in the governing equations, respectively. Details of these numerical schemes can be found in [39]. The conjugate heat transfer problem is solved in ANSYS CFX 15.0 based one finite element based finite volume method and time marching algorithm [39]. A solution is considered to be converged when (a) the normalized residuals for all the governing equations are less than 10^{-6} and (b) representative parameters (e.g., average temperature on the heated substrate surface) remain constant within at least 200 iterations.

Mesh independency test is carried out at the highest Reynolds number considered in the present study. For the rectangular honeycomb, three meshes separately with 1.32 million, 1.92 million and 2.32 million elements are considered; the predicted overall Nusselt numbers and friction factors from these three meshes exhibit a deviation less than 0.3%. For the X-lattice sandwich panel, three meshes separately with 11.6 million, 18.8 million and 29.8 million elements are considered; the predicted overall Nusselt numbers and friction factors from these meshes show a discrepancy less than 2.1%. For the X-lattice cored honeycomb, two meshes separately with 17.4 million and 33.8 million elements are generated; the overall Nusselt numbers and friction

factors from these two meshes show a deviation less than 1.6%. To balance the computational cost and numerical accuracy, meshes with 1.32 million, 11.6 million and 17.4 million elements are finally used for the rectangular honeycomb, the X-lattice sandwich panel and the X-lattice cored honeycomb, respectively.

4. DISCUSSION OF RESULTS

4.1. Enhanced overall heat transfer

Since the overall heat transfer performance of the PCMs is the first concern in terms of engineering applications, it is considered first. Figs. 6(a) and 6(b) present the streamwise profile of overall Nusselt number (Nu) for the PCMs separately made of the Inconel 718 stainless steel and aluminium at the highest Reynolds number considered in the present study. When the solid thermal conductivity (k_s) is 11.4 W/(mK), the three PCMs exhibit different trends. For the rectangular honeycomb, Nusselt number first decreases and finally approaches a constant value due to gradual development of the flow and thermal boundary layers; the entry effect is obvious but no exit effect is observable. On the contrary, for the X-lattice sandwich panel, the Nusselt number within the first two unit cells is evidently lower than that in the rest unit cells due to insufficient development of the complex primary and secondary flows [28]. As a result of the above two effects, the profile of Nusselt number for the X-lattice cored honeycomb seems to be a horizontal line, without obvious entry and exit effects. Quantitatively, the Nusselt number for the X-lattice cored honeycomb is 90~190% and 30~50% higher than that of the rectangular honeycomb and X-lattice sandwich panel, respectively. Furthermore, the numerical and experimental results for the X-lattice cored honeycomb agree well, showing a maximum deviation of 5.6%.

With the increase of material thermal conductivity, the streamwise profile of Nusselt number changes as revealed by Fig. 6(b) when the thermal conductivity of solid (k_s) is 236 W/(mK). With a constant heat flux imposed on the substrate, the fluid temperature increases monotonically along the flow direction. Correspondingly, the substrate temperature also increases along mainstream. Hence, heat conduction will take place from the hotter solid to the cooler solid in the bottom substrate, i.e., in the opposite direction to the fluid flow. In such a situation, the solid material closer to the PCM inlet acts as additional extended surface to the substrate section away from the PCM inlet; overall Nusselt number for these unit cells increases. As a result of the above reasons, the entry effect for the rectangular honeycomb diminishes, while a monotonic increase of overall Nusselt number along the flow direction is observable for the X-lattice sandwich panel and the X-

lattice cored honeycomb. Quantitatively, the Nusselt number for the X-lattice cored honeycomb is 250~450% and ~40% higher than that of the rectangular honeycomb and X-lattice sandwich panel, respectively. Since the heat transfer coefficient on the surface of the new PCM is expected to be higher than that of the rectangular honeycomb, the fin efficiency of the new PCM increases more rapidly with the increase of material thermal conductivity. Hence the superiority of the new PCM relative to the rectangular honeycomb drastically increases.

Before comparison of the overall heat transfer at various Reynolds numbers, the numerical models are carefully validated. For validating the model for the bare honeycomb, a similar problem, i.e., convective heat transfer in a rectangular channel is simulated due to lack of the experimental data for the honeycomb within the present Reynolds number range. To this end, the numerical model for the rectangular honeycomb as shown in Fig. 5(a) is modified; the solid walls of the honeycomb are replaced by a no-slip wall with zero thickness; constant heat flux is applied to the wall; and a uniform flow velocity is specific at the inlet of the computational domain. Fig. 7(a) compares the area-averaged Nusselt number (Nu_H) numerically predicted with that calculated by the well-recognized Gnielinski equation [40]. It should be noted that the original Gnielinski equation takes the hydraulic diameter of the tube as the characteristic length scale instead of the channel height in the present study. Therefore, the equation is modified and has the following form:

$$Nu_H = \frac{w \cdot H_c}{2w} \frac{\left(\frac{1}{8}\frac{2w}{w \cdot H_c} f_H\right)\left(Re_H - 1000\right)Pr}{1 + 12.7\sqrt{\frac{1}{8}\frac{2w}{w \cdot H_c} f_H}\left(Pr^{2/3} - 1\right)} \left[1 + \left(\frac{2wH_c}{w \cdot H_c L}\right)^{2/3}\right] \tag{7}$$

where Nu_H is the area-averaged Nusselt number based on the height (H_c) of the channel; Re_H and f_H are separately defined in Eq. (2) and Eq. (6) with $t_f = 0$; Pr is the Prandtl number of air. The friction factor (f_H) for fully developed flow is calculated by the Blasius equation expressed as follows [41, 42]:

$$f_H = 0.3164 \left(\frac{w \cdot H_c}{2w} \frac{2w}{w \cdot H_c} Re_H\right)^{-0.25} \tag{8}$$

For the empty rectangular channel, it is demonstrated by Fig. 7(a) that the deviation is more than 15% at the first two Reynolds numbers since the flow is within the transitional flow regime. As pointed out by Abraham et al. [37], the shear stress transport turbulence model generally over predict the heat transfer performance within this regime. For the rest data points, the deviation gradually decreases with increasing Reynolds number, showing an acceptable discrepancy less than 11.6%. For the other two PCMs, Fig. 7(a) reveals that the

deviations between the numerical and the experimental data are less than 12% and 3%, respectively.

After the validation of the numerical model, the overall Nusselt number (Nu_H) is calculated based on the Nusselt numbers in the unit cells of each PCM as those shown in Fig. 6 and is plotted in Fig. 7(b). When the Inconel 718 Alloy is used to fabricate the PCMs, the overall Nusselt number for the new PCM is ~170% and ~55% higher than those for the bare honeycomb and X-lattice, respectively. When aluminium is used for fabrication, the superiority is 340~360% and 26-40%, respectively.

4.2. Fluid flow characteristics

In consideration of the evident difference on overall heat transfer among the three PCMs, it is useful for the invention of more advanced PCMs to get insight into detailed mechanisms underlying the mutual thermo-fluidic effects between the X-lattice and the rectangular honeycomb. To this end, the fluid flow is analysed first, which is the basis of local heat transfer analysis.

In order to clearly present the complex large-scale separated flow and heat transfer in the X-lattice sandwich panel and the X-lattice cored honeycomb, the lattice ligaments, flow area and the endwall of each unit cell are carefully classified into different types as schematically shown in Fig. 8. To facilitate the following descriptions, coordinate system is also included in the figure. The two ligaments of each unit cell are called ligament A and B, respectively. They are separately inclined to the downstream and upstream directions from the bottom endwall at $y = 0$ mm. In each unit cell, the fluid flow approaching ligament A is divided into three streams passing cross-sections A, B and C, respectively. Similarly, the three flow areas around ligament B are denoted as cross-sections D, E and F, respectively. The bottom endwall region at $x < 0$ and the upper endwall region at $x > 0$ are denoted as area A, while the rest endwall regions are denoted as area B. Readers are kindly suggested to refer to Fig. 8 for easier understanding the following complex flow and heat transfer characteristics.

4.2.1. Bulk flow, vortex structures and turbulence field

Figs. 9•••• present the bulk flow characteristics, where plenty of three-dimensional streamlines are released from the representative flow areas as depicted in Fig. 8. The simple parallel flow in the bare honeycomb is not included for brevity. Due to the periodic nature of the PCMs, the flow becomes fully developed after a short entrance region. Therefore, the fully developed flow after the fifth unit cell is selected

and presented. For the X-lattice sandwich panel, it is found that the fluid flows downstream cross-sections A, B and C are correspondingly the same as those downstream cross-sections D, E and F, respectively. Therefore, only the streamlines through cross-sections A, B and C as shown in Fig. 9 are analyzed. For the X-lattice cored honeycomb, however, the flows downstream these six cross-sections as shown in Figs. 10(a)-(f) are different from one another.

As reference, fluid flow in the X-lattice sandwich panel is discussed first. It is calculated that the mass flow rate through cross-section A accounts for 13% of the total mass flow rate in this sandwich panel. As revealed by Fig. 9(a), some fluid passing cross-section A of the unit cell is forced to flow upward, leftward, downward and rightward in sequence as a result of the blockage by the downstream ligaments arranged in a spiral topology; thus, a large-scale spiral flow takes place. At the leeside of the sharp-edged ligament A, a low pressure wake region is expected to form; consequently, some fluid through cross-section A is driven to impinge on the leeside of ligament A by pressure difference, finally turning into a pair of counter-rotating vortices as shown in Fig. 9(a). When the bulk fluid through cross-section B passes the bottom endwall, it is separated due to continuous development of the boundary layer and adverse pressure gradient as a result of flow stagnation near the y-z plane at $x = -w$; hence, a separation vortex is induced near the passage corner at $(x, y) = (-0.5w, 0)$ as revealed by the right figure in Fig. 9(a). Part of the fluid through cross-section A is also transported to the leeside of ligament B in the same unit cell and impinges on the backside of the ligament B, forming two legs of the counter-rotating vortex pair as revealed by the right figure in Fig. 9(a). The mass flow rate through cross-section B is much higher than those through the other two cross-sections, accounting for 77% of the total mass flow rate; therefore, this stream as shown in Fig. 9(b) is the most important contributor to the large-scale spiral flow due to the spiral topology of the X-lattice. Some fluid is also forced to the leeside of the ligament A and B in the same unit cell and significantly contributes to the vortex pair there. Due to similar reasons, a flow separation vortex near the passage corner at $(x, y) = (0.5w, H_c)$ similar to that near the bottom endwall is observable in Fig. 9(b). The mass flow rate through cross-section C accounts for 10% of the total mass flow rate. As shown in Fig. 9(c), this stream is completely skewed towards the positive x direction after passing the cross-section C and feeds fluid to the leeside of ligament B, contributing to the the local vortex pair.

Corresponding to the streamlines in Fig. 9, visualization of the vortex structures in the X-lattice sandwich panel is presented in Fig. 12(a) by using the iso-surfaces of the positive second invariant of the velocity gradient

tensor according to the *Q*-criterion [43]. It should be noted that the reasonability of the vortex extraction method is generally case-dependent. In particular, the vortices in this paper extracted by the *Q*-criterion are found to be reasonable based on careful validation with streamlines. It can be seen in Fig. 12(a) that the shape and location of the vortices downstream ligaments A and B are almost the same. The legs of the counter-rotating vortex pair generated from the stream through cross-sections B or E are finally merged with a large longitudinal vortex, which dominates the bulk flow. As marked in Fig. 12(a), the centreline of the longitudinal vortex downstream ligament A is ~0.62H_c and ~0.36w away from the bottom endwall and the y-z plane at x = -0.5w, respectively. In comparison, the other leg of each vortex pair at the leeside of each ligament and the separation vortices near the endwalls are relatively much smaller.

The special bulk flow and vortices in the X-lattice sandwich panel lead to unique production, transportation and dissipation of the turbulent kinetic energy, resulting in the spatial distribution as exhibited by the contours in Fig. 9 and Fig. 12(a). According to available experimental and DNS investigations on the separated turbulent flow past bluff blunt bodies [44-46], the turbulence production at the vicinity of the vortex boundary is the highest due to strong shear and interaction between the high-velocity and the low-velocity fluids separately outside and inside the vortex cores, while the turbulence dissipation there is relatively moderate. In addition, the vortex induced turbulence is generally much stronger than that induced by the fluid shear in the wall boundary layer, while the fluid shear in the sub-layer of the wall boundary layer leads to rapid dissipation of turbulent kinetic energy. Specifically for the present X-lattice sandwich panel, it is demonstrated by the contours in Fig. 9 and Fig. 12(a) that the counter-rotating vortex pair is the main source of turbulent kinetic energy. As shown in Fig. 9(a), the fluid passing the cross-section A is broadly divided into two streams, i.e., the vortex behind ligament A and the high-velocity flow around it; strong shear and interaction between these two streams leads to high turbulent kinetic energy around the intersection point of the ligaments; subsequently, as a result of the spiral flow pattern, the turbulent kinetic energy is transported to the endwalls mainly by convection. Similarly, high turbulent kinetic energy is also induced at the vicinity of the vortex from the fluid through cross-section B as shown by the left figure in Fig. 9(b), which also contributes to the local high turbulent kinetic energy near the endwalls mainly by diffusion. For the stream through the cross-section C as shown in Fig. 9(c), the local high turbulent kinetic energy region is mainly induced by the diffusion of the turbulent kinetic energy from the rest fluid. In comparison, the turbulent kinetic energy in the wall boundary layer is very low due to rapid dissipation by molecular viscosity.

Based on the above understanding of the turbulent flow in the X-lattice sandwich panel, the similar and dissimilar characteristics in the X-lattice cored honeycomb is subsequently explored. It is calculated that the mass flow rates through cross-sections A, B and C (or D, E and F) of the X-lattice cored honeycomb are almost identical to those through cross-sections A, B and C of the X-lattice sandwich panel. Therefore, the introduction of the honeycomb walls does not significantly change the distribution of the coolant through these cross-sections. However, the flow pattern is evidently modified by the honeycomb walls. Fig. 10 and Fig. 11 separately present the fluid flows through cross-sections A, B and C as well as that through cross-sections D, E and F in the X-lattice cored honeycomb, which are different from one another. Similar to the fluid flow in the X-lattice sandwich panel, a large-scale spiral flow is clear in the X-lattice cored honeycomb as revealed by Figs. 10 and 11. The streams through cross-sections A and B feed fluid to the leeside of the ligament A, leading to the local counter rotating vortex pair which is then merged with a large longitudinal vortex as revealed by Figs. 10(a) and 10(b). Similarly, a counter rotating vortex pair is observable behind ligament B as revealed by Figs. 11(a) and 11(b). In particular for the X-lattice cored honeycomb, several unique flow features exist as detailed below. First, the formation and development of the flow boundary layer on the honeycomb walls enlarges the separation vortex near the corners at $(x, y) = (-0.5w, 0)$ as revealed by Fig. 10(a) and $(x, y) = (0.5w, H_c)$ as revealed by Fig. 10(b), respectively. In addition, two new separation vortices near the corners separately at $(x, y) = (-0.5w, H_c)$ as shown in Fig. 10(a) and $(x, y) = (0.5w, 0)$ as shown in Fig. 10(b) are induced due to continuous development of the boundary layer on the honeycomb walls and flow stagnation near the x-z planes at $y = H_c$ and $y = 0$, respectively. Second, the vortex flows near the leeside of the ligament A are different from those of the ligament B, in contrast to the similar vortex flows behind all the ligaments in the X-lattice sandwich panel. As revealed by the streamlines in Figs. 10(a) and 10(b), both the streams from cross-section A and cross-section B significantly contributes to the counter-rotating vortex pair near the leeside of the ligament A; in comparison, the leg of the vortex pair from the stream through cross-section E only touches a small portion of the leeside of the ligament B as shown in Fig. 11(b), while vortex flow near the leeside is mainly dominated by the stream through cross-section D where a new big separation vortex forms near the top section of the ligament as shown in Fig. 11(a). Finally, by comparing the streamlines through cross-section C or D between the X-lattice sandwich panel as shown in Fig. 9(c) and the X-lattice cored honeycomb as shown in Figs. 10(c) and 11(c), it can be concluded that the formation of the flow boundary layer on the honeycomb walls and the correspondingly enlarged and newly induced separation vortices weakens the tangential flow near the endwalls

and the honeycomb walls.

Corresponding to the streamlines in Figs. 10 and 11, Fig. 12(b) presents the vortex structures in the X-lattice cored honeycomb. Similar to the X-lattice sandwich panel, the counter-rotating vortex pairs behind the ligaments dominate the vortex structure; separation vortices near the corners separately at (x, y) = (-0.5w, 0) and (x, y) = (0.5w, H_c) are also clear. In particular, the X-lattice cored honeycomb exhibits several unique features as detailed below. In contrast to the almost identical vortices behind all the ligaments as shown in Fig 12(a), the vortex structure seems to repeat every two unit cells as shown in Fig. 12(b). As revealed by the top figure in Fig. 12(b), the counter-rotating vortices flow all the way along the leeside of ligament A with the leg from the cross-section B turning into a longitudinal vortex which is much stronger than the other leg. Behind the ligament B, however, the leg of the vortex pair from the cross-section E flows far away from the backside surface of the ligament B once generated as revealed by the bottom figure in Fig. 12(b); thus a new separation vortex forms behind the ligament in addition to the other leg of the vortex pair as revealed by the streamlines in Figs. 11(a) and 11(c). Further, more separation vortices is clear near the four corners of the flow passage and the honeycomb walls, which is much bigger than the separation vortices near the endwalls of the X-lattice sandwich panel.

To further elucidate the significantly distinctive vortices downstream the ligaments between these two PCMs, pressure distributions on several representative planes corresponding to the sixth and the seventh unit cells are extracted as shown in Fig. 13, where p and p_{min} is the local pressure and minimum pressure on each plane, respectively. Detailed analysis of the vortex development from the inlet to the outlet of the computational domain reveals that the fluid first approaches ligament A of the lattice unit cell and results in the vortices behind ligament A. As marked in Fig. 12(b), the longitudinal vortex behind ligament A of the X-lattice cored honeycomb is closer to the top endwall and further from the plane at x = -0.5w compared that of the X-lattice sandwich panel, which is possibly caused by the blockage of the newly generated and enlarged separation vortices compared to the X-lattice sandwich panel. Correspondingly, the low pressure region induced by this longitudinal vortex in the X-lattice cored honeycomb is closer to the root vertex of ligament B compared to that of the ligament A as revealed by the comparison between Fig. 13(a) and Fig. 13(b); thus stronger entrainment of the fluid near the root of the ligament B in the X-lattice cored honeycomb is expected, which forces the vortex behind ligament B flow far away from the leeside as revealed by the bottom figure in Fig. 12(b). Subsequently, the effect of the longitudinal vortex behind ligament B on the root region of the

ligament A becomes similar to that of the X-lattice sandwich panel and leads to similar counter-rotating vortices flowing close to the leeside of the ligament A as revealed by the top figure in Fig. 12(b).

The modification of the fluid flow by the presence of honeycomb walls results in a distinctive spatial distribution of the turbulent kinetic energy as depicted by the contours in Figs. 10, 11 and 12(b). Similar to the X-lattice sandwich panel, strong shear near the vicinity of the counter-rotating vortices downstream the ligaments is the main source of turbulent kinetic energy production. However, its transport and dissipation is significantly affected by the no-slip honeycomb walls. For the X-lattice sandwich panel, the planes at $x = \pm 0.5w$ are symmetric planes; the local gradients of all the variables are zero, which leads to weak dissipation of the turbulent kinetic energy. For the X-lattice core honeycomb, however, the planes at $x = \pm 0.5w$ are no-slip walls where strong dissipation dominates; therefore, the vortex induced turbulent kinetic energy is quickly dissipated with the proceeding of its convection and diffusion. Therefore, the turbulent kinetic energy magnitude in the X-lattice cored honeycomb is drastically reduced.

4.2.2. Local flow behaviors

Corresponding to the above bulk flow characteristics, local fluid flow dominating the local heat transfer patterns on the surfaces are explored below. Fig. 14 first depicts the tangential flow behaviours by the surface streamlines and tangential velocity contours on several representative planes. For each PCM, the qualitative characteristics in the x-y planes, i.e., planes 1 to plane 5, are similar; hence the flow on plane 3 is selected as a representative for the analysis below. For the X-lattice sandwich panel, the fluid near the symmetry plane at $x = -0.5w$ flows smoothly towards the endwall and stagnates there without flow separation as revealed by the surface streamlines in Fig. 15(a); for the X-lattice cored honeycomb, however, the flow separates near the upper section of the honeycomb wall at $x = -0.5w$ and changes the flow direction; therefore, the static pressure near the corner at $(x, y) = (-0.5w, H_c)$ of the X-lattice cored honeycomb is expected to be lower than that of the X-lattice sandwich panel due to less prominent flow stagnation. After changing the flow direction, the flow separates near the corner at $(x, y) = (0.3w, H_c)$; more severe flow separation for the X-lattice cored honeycomb induces a bigger separation vortex and leads to more prominent blockage to the fluid flow; therefore, the local static pressure near the corner at $(x, y) = (0.3w, H_c)$ of the X-lattice cored honeycomb is expected to be higher than that of the X-lattice sandwich panel. Due to the above two reasons, the transverse pressure difference along the positive x-direction of the X-lattice cored honeycomb is evidently lower than that of the X-lattice

sandwich panel as revealed by Fig. 13, which is disadvantageous to the tangential acceleration of the fluid in the boundary layer over the endwall. As a result, the high-tangential velocity flow is further away from the endwall of the X-lattice cored honeycomb compared to the X-lattice sandwich panel as demonstrated by the tangential velocity contours on planes 1–5 in Fig. 14. Correspondingly, the flow downstream the joint between the ligament and the endwall spreads more quickly in the X-lattice sandwich panel than that in the X-lattice cored honeycomb as revealed by the surface streamlines on plane 6. In addition, the formation of the flow boundary layer and newly generated/enlarged flow separation vortices near the honeycomb walls lower local tangential flow velocity and thickens the flow boundary layer as revealed by the contours on plane 7.

Fig. 15 then presents the contours of velocity magnitude on several planes placed 0.1 mm away of the adjacent walls or the symmetry planes. Under the centrifugal effect of the spiral flow pattern and the complex secondary flows, the flow velocity near the four boundaries of the square flow passage in the X-lattice sandwich panel and the X-lattice cored honeycomb is much higher than that of the rectangular honeycomb. According to the velocity distributions on plane 6 in Fig. 15, it can be concluded that the lower tangential velocity downstream the joint endows the X-lattice cored honeycomb with a bigger low-velocity wake region. Comparison of the velocity distributions on plane 7 reveals that the thickened boundary layer near the honeycomb walls of the X-lattice cored honeycomb lowers local flow velocity.

Fig. 16 finally presents the distributions of turbulent kinetic energy on the aforementioned planes. It can be seen that the X-lattice induced turbulence is much stronger than that of the rectangular honeycomb. More interestingly, the presence of the no-slip honeycomb walls significantly reduces the local turbulent kinetic energy in plane 7 due to severe dissipation by the boundary layer flow. Such low turbulence fluid is then transported to the endwall by convection of the spiral flow. For the X-lattice sandwich panel, however, the vortex generated high turbulent kinetic energy is transported to the endwall by the spiral flow because the turbulence dissipation is limited due to zero gradients of all the variables on the symmetry plane. Further, corresponding to the stronger tangential flow on plane 6 of the X-lattice sandwich panel as shown in Fig. 14, more high turbulence fluid spreads and covers a large portion of the endwall (i.e., area B in Fig. 8).

4.3. Local heat transfer characteristics

The different turbulent flow behaviours as clarified above result in different local heat removals from the endwalls, the lattice ligaments and the honeycomb walls, which are responsible for the overall heat transfer

performance. Detailed comparisons of the local heat transfer among these three PCMs are presented below.

4.3.1. Local heat transfer on the endwall

Figs. ••••••••first present the local heat transfer distribution on the bottom endwall of the three PCMs as indicated by the local Nusselt number (*Nu*) based on local heat flux, wall temperature and bulk mean fluid temperature. For the rectangular honeycomb as shown in Fig. 17(a), when the fully developed flow between two parallel plates enters the flow channels, the flow and thermal boundary layers redevelop. Hence the Nusselt number at the entrance section is relatively higher due to thinner boundary layer; then the Nusselt number gradually decreases and approaches a constant distribution.

For the X-lattice sandwich panel as shown in Fig. 17(b), however, the local Nusselt number in the first two unit cells is significantly lower than that in the downstream unit cells; this implies that heat transfer in this PCM is dominated by the complex flow mixing via vortex flow induced by the X-lattice. When the fully development parallel flow enters this PCM, it gradually changes the flow pattern under the effect of the ligaments until a new fully developed flow pattern builds up, which gradually intensifies flow mixing by the complex vortex flows. Therefore, the Nusselt number gradually increases and approaches a constant value along the flow direction. It can also be observed in Fig. 17(b) that heat transfer on area B of the endwall is significantly superior to that on area A, which attributes to the velocity and turbulent kinetic energy distributions in Figs. 15 and 16. As previously discussed, strong tangential flow near the endwall helps to spread the high-velocity fluid over area B as indicated by the velocity magnitude counter in Fig. 15(b), while a large low-velocity wake predominates over area A. In addition, the vortex-induced high turbulent kinetic energy is transported to area B and spread over it, while the turbulent kinetic energy over area A is much lower as shown in Fig. 16(b). The specific heat transfer distribution on area A and area B is a result of the above two effects.

For the X-lattice cored honeycomb, the effect of the no-slip honeycomb walls gradually accumulates. The local heat transfer pattern within the first unit cell is similar to that of the X-lattice sandwich panel due to insufficient influence by the honeycomb walls. Further downstream, the local heat transfer pattern gradually differs from that in the X-lattice sandwich panel. It can be seen that heat transfer on area B of the sandwich panel is significantly deteriorated by the honeycomb walls. As revealed by Fig. 15, the weakened tangential flow by the honeycomb walls limits the transport and spread of the high-velocity flow to the wake region and

consequently results in a bigger low-momentum wake region; in addition, the presence of the honeycomb walls also significantly reduces the turbulent kinetic energy magnitude over area B as revealed by Figs. 16(b) and (c). As a result of the above two points, local heat transfer on area B is deteriorated. The heat transfer on area A of the X-lattice cored honeycomb is quantitatively close to that of the X-lattice sandwich panel due to similar velocity and turbulent kinetic energy magnitude as shown in Figs. 15 and 16.

Fig. 17(d) presents a quantitative comparison of the heat transfer on the endwall among these three PCMs, where Nu_{ave} represents the area-averaged Nusselt number obtained by integrating the counters in Figs. ••••• ••••••••••• It is calculated that the average Nusselt number for the X-lattice cored honeycomb is approximately 30% lower than that for the X-lattice sandwich panel. Due to limited flow mixing in the rectangular honeycomb, average Nusselt number for the X-lattice sandwich panel and the X-lattice cored honeycomb is approximately 3 times and 1.9 times higher than that of the rectangular honeycomb, respectively.

4.3.2. Local heat transfer on the ligament

Figs. 18(a) and 18(b) illustrate the local heat transfer patterns on the ligaments of the PCMs where the local Nusselt number is defined in the same way as that in Fig. 17. For the X-lattice sandwich panel, the heat transfer pattern repeats every single unit cell after the entry region as shown in Fig. 17(a), while the distribution for the X-lattice cored honeycomb repeats every two unit cells as shown in Fig. 17(b). On the upstream surfaces of the ligaments, the Nusselt number for the X-lattice cored honeycomb is slightly lower than that of the X-lattice sandwich panel partially due to significantly reduced bulk turbulent kinetic energy magnitude. On the downstream surface of the ligament A, both PCMs exhibit similar magnitude and distribution of Nusselt number; on the downstream surface of the ligament B, however, the area of the arc-shaped high heat transfer region is evidently reduced by the honeycomb walls because the dominant leg of the counter-rotating vortex pair moves away from the leeside of ligament B as shown in Fig. 12(b). Overall, the heat transfer on the downstream surface of the X-lattice cored honeycomb is lower than that of the X-lattice sandwich panel. As quantified in Fig. 18(c), the average Nusselt number is reduced by 6% to 9% within the present Reynolds number range.

4.3.3. Local heat transfer on the honeycomb wall

Fig. 19 finally highlights the influence of the X-lattice on local heat transfer on the honeycomb walls. For

the bare rectangular honeycomb, a similar heat transfer pattern to that on its endwall is observable due to rebuild and gradual development of the boundary layer. In comparison, it is clear that the heat transfer of the X-lattice cored honeycomb is much higher than that of the rectangular honeycomb due to higher velocity and turbulent kinetic energy as shown in Figs. 15 and 16. For the X-lattice cored honeycomb, in particular, Nusselt number as high as 150 to 180 presents at the upper region of the honeycomb wall; flow reattachment due to the separation vortex near the corner at $(x, y) = (0.5w, H_c)$ (see Fig. 14(c)) and the corresponding high velocity and turbulent kinetic energy are responsible for the superior heat transfer. Further downstream along the negative y-direction, the Nusselt number decreases due to development of the boundary layer and the decay of turbulence as shown in Figs. 15 and 16. As quantified in Fig. 19(b), the introduction of X-lattice enhances the average Nusselt number on the honeycomb walls by approximately 2.3 times.

4.4. Pressure drop

As an important performance index for thermal management or heat exchange systems, pressure drop of the new PCM is considered. Fig. 20(a) first compares the numerical results with the experimental or empirical data; the deviation is less than 5.2%, 11.4% and 9.6% separately for the empty square channel, the X-lattice and the rectangular honeycomb, which is acceptable.

To ensure a meaningful comparison among the three PCMs, the entry and exit effects on the pressure drop must be clarified. Therefore, Figs. 20(b-d) show the streamwise variation of pressure coefficient (C_p) defined as:

$$C_p = \frac{p(0, H_c, z) - p(0, H_c, H_c)}{\frac{1}{2}\left(1 - \frac{t_f}{w}\right) U_{mc}^2} \tag{9}$$

Severe entry and exit effects separately due to abrupt contraction and expansion are observable for the rectangular honeycomb as revealed by Fig. 20(b). For the rest two PCMs, such effects are negligible; the curves show a periodic pattern corresponding to the geometric periodicity.

Fig. 20(e) finally compares the friction factors among the three PCMs. For the rectangular honeycomb, the friction factor is calculated based on the pressure drop from $z/L = 0.1$ to $z/L = 0.9$ to eliminate the entry and exit effect. It is demonstrated that the friction factor for the X-lattice cored honeycomb is higher than that of the rectangular honeycomb as expected. The intergration of honeycomb with the X-lattice slightly increases

the pressure drop by ~16% mainly due to additional friction loss from the increased surface area.

4.5. Overall thermal performance

In light of the fact that the integration of the rectangular honeycomb to the X-lattice leads to increased overall Nusselt number and pressure drop penalty concurrently, it is necessary to evaluate and compare the heat transfer performance under the fixed pumping power condition. As argued by Tian et al. [14], the pumping power consumption for transporting the fluid is proportional to the non-dimensional parameter $f_H Re_H^3$ [28], while heat transfer is proportional to the overall Nusselt number Nu_H. Therefore, Fig. 21 presents the Nu_H as a function of $f_H Re_H^3$. It can be seen that the X-lattice cored honeycomb is superior, showing a 33-42% and 21-34% higher Nusselt number at fixed pumping power when the material thermal conductivity is 11.4 W/(mK) and 236 W/(mK), respectively.

5. CONCLUSIONS

To further improve the mechanical strength and the heat dissipation performance of the X-lattice, a new periodic cellular material called "X-lattice cored rectangular honeycomb" is devised by integrating the X-lattice with the rectangular honeycomb. Overall heat transfer and pressure drop as well as detailed turbulent flow and local heat transfer mechanisms are clarified in this paper. Conclusions obtained based on the above analysis are summarized below.

(1) Under fixed Reynolds number conditions within the range of ••••••••••when these PCMs are made of the Inconel 718 stainless steel with a low thermal conductivity of 11.4 W/(mK), the superiorities of this new PCM relative to the parent rectangular honeycomb and the X-lattice sandwich panel are up to 170% and 55%, respectively. When they are made of the aluminium with a high thermal conductivity of 236 W/(mK), the superiorities are up to 360% and 40%, respectively.

(2) For the X-lattice sandwich panel, in addition to the spiral flow and secondary flow patterns uncovered in our previous studies, new insight into the flow mechanisms dominating local heat transfer is found in this study. It is found that strong shear near the vicinity of the counter-rotating vortex pair behind the ligament is the dominant source of turbulent kinetic energy, which is effectively transported to the endwalls by convection and diffusion.

(3) The introduction of the honeycomb walls into the X-lattice sandwich panel significantly modifies the

turbulent flow patterns. First, in contrast to smooth flow on symmetry plane between the adjacent lattice unit cells in the X-lattice sandwich panel, new separation vortices are induced due to formation and development of flow boundary layer on the newly added honeycomb walls; in addition, existing separation vortices near the endwalls are also enlarged by the honeycomb walls; consequently, the tangential flow perpendicular to the mainstream is weakened due to variation of the flow stagnation conditions near the four corners of the square flow channel. Second, the blockage imposed by the newly generated/enlarged separation vortices modifies the vortex pairs behind the ligaments, with one dominant leg of the vortex pair downstram ligament B moves away from the leeside of these ligaments; in addition, the vortex flow pattern repeats every two unit cells in the X-lattice cored honeycomb in contrast to the almost identical vortex flow in all the unit cells of the X-lattice sandwich panel. Finally, the presence of the no-slip honeycomb walls significantly reduces the bulk turbulent kinetic energy magnitude in the flow and restricts its transport to the endwalls due to severe dissipation by the viscous sub-layer and the deteriorated tangential flow.

(4) The corresponding reduction of tangential flow velocity and the turbulent kinetic energy near the endwalls due to the no-slip honeycomb walls reduces the heat transfer on the endwall by approximately 30%. The reduced shear by the dominant leg of the vortex pair behind the ligament B and turbulent kinetic energy deteriorate the heat transfer on the ligaments by up to 9%. However, intensified flow mixing, increased local flow velocity and flow mixing induced high turbulent kinetic energy near the honeycomb walls drastically enhance the heat transfer on the honeycomb walls by 2.3 times.

(5) The introduction of the honeycomb walls leads to a ~16% higher friction factor. However, under fixed pumping power conditions, the new X-lattice cored honeycomb provides up to 42% and 34% higher heat transfer than the X-lattice sandwich panel when Inconel 718 alloy and aluminium is used for the fabrication of the PCMs, respectively.

ACKNOWLEDGEMENTS

This research was supported by the National Key Research and Development Program of China (2017YFB1102801), the National Natural Science Foundation of China (51806176), the Natural Science Basic Research Plan in Shaanxi Province of China (2018JQ5159), the Research Fund of Key Laboratory of Aircraft Environment Control and Life Support, MIIT, Nanjing University of Aeronautics and Astronautics (KLAECLS-E-201901), the Fundamental Research Funds for the Central Universities (3102018zy004), the

111 Project (B18041), the Open Project for Key Laboratory of Intense Dynamic Loading and Effect (KLIDLE1801) and the Aviation Science Foundation Project (20170970002).

REFERENCES

[1] H.N.G. Wadley, Multifunctional periodic cellular metals, Philos. Trans. Roy. Soc. A 364 (1838) (2006) •••••••••••

[2] L. Ferrari, M. Barbato, B. Esser, I. Petkov, M. Kuhn, S. Gianella, J. Barcena, C. Jimenez, D. Francesconi, V. Liedtke, A. Ortona, Sandwich structured ceramic matrix composites with periodic cellular ceramic cores: an active cooled thermal protection for space vehicles, Compos. Struct. 154 (2016) •••••••••••

[3] S.S. Feng, M.Z. Li, J.H. Joo, K.J. Kang, T. Kim, T.J. Lu, Thermomechanical properties of brazed wire-woven bulk Kagome cellular metals for multifunctional applications, J. Thermophys. Heat Transfer 26 (1) (2012) •••••••••••

[4] H.B. Yan, Q.C. Zhang, T.J. Lu, Heat transfer enhancement by X-type lattice in ventilated brake disc, Int. J. Therm. Sci. 107 (2016) 39±55.

[5] K.J. Kang, Wire-woven cellular metals: the present and future, Prog. Mater. Sci. 69 (2015) ••••••••••••

[6] A. Merabtine, N. Gardan, J. Gardan, H. Badreddine, C. Zhang, F. Zhu, X.L. Gong, 2018. Experimental and numerical thermal analysis of open-cell metal foams developed through a topological optimization and 3D printing process. Eur. Phys. J. Appl. Phys. 83, 10904.

[7] T. Wen, J. Tian, T.J. Lu, D.T. Queheillalt, H.NG. Wadley, Forced convection in metallic honeycomb structures, Int. J. Heat Mass Transfer 49 (19) (2006) ••••••••••••••

[8] J. Tian, T.J. Lu, H.P. Hodson, D.T. Queheillalt, H.N.G. Wadley, Cross flow heat exchange of textile cellular metal core sandwich panels, Int. J. Heat Mass Transfer 50 ••••••••(2007) ••••••••••••••

[9] J.H. Joo, K.J. Kang, T. Kim, T.J. Lu, Forced convective heat transfer in all metallic wire-woven bulk Kagome sandwich panels, Int. J. Heat Mass Transfer 54 (25-26) (2011) ••••••••••••••

[10] T. Kim, C.Y. Zhao, T.J. Lu, H.P. Hodson, Convective heat dissipation with lattice-frame materials, Mech. Mater. 36 (8) (2004) ••••••••••••

[11] F. Hoffmann, Heat Transfer Performance and Pressure Drop of Kagome Core Metal Truss Panels, Cambridge University Press, Cambridge, 2002.

[12] H.N.G. Wadley, N.A. Fleck, A.G. Evans, Fabrication and structural performance of periodic cellular

metal sandwich structures, Comp. Sci. Technol. 63 (16) (2003) ••••••••••••••••

[13] Q.C. Zhang, Y.J. Han, C.Q. Chen, T.J. Lu, Ultralight X-type lattice sandwich structure (I): concept, fabrication and experimental characterization, Sci. China Ser. E: Tech. Sci. 52 (8) (2009) ••••••••••••••••

[14] J. Tian, T. Kim, T.J. Lu, H.P. Honson, D.T. Queheillalt, D.J. Sypeck, H.N.G. Wadley, The effects of topology upon fluid-flow and heat-transfer within cellular copper structures, Int. J. Heat Mass Transfer 47 (14) (2004) ••••••••••••••••

[15] J.Y. Ho, K.C. Leong, T.N. Wong, Experimental and numerical investigation of forced convection heat transfer in porous lattice structures produced by selective laser melting, Int. J. Therm. Sci. 137 (2019) ••••••••••••••••

[16] G.W. Kooistra, H.N.G. Wadley, Lattice truss structures from expanded metal sheet, Mater. Des. 28 (2) (2007) ••••••••••••••••

[17] T. Kim, H.P. Hodson, T.J. Lu, Pressure loss and heat transfer mechanisms in a lattice-frame structured heat exchanger, IMechE J. Mech. Eng. Sci. 218 (11) (2004) ••••••••••••••••

[18] T. Kim, H.P. Hodson, T.J. Lu, Fluid-flow and endwall heat-transfer characteristics of an ultralight lattice-frame material, Int. J. Heat Mass Transfer 47 (6) (2004) ••••••••••••••••

[19] T. Kim, H.P. Hodson, T.J. Lu, Contribution of vortex structures and flow separation to local and overall pressure and heat transfer characteristics in an ultralightweight lattice material, Int. J. Heat Mass Transfer 48 (19) (2005) ••••••••••••••••

[20] L. Gao, Y.G. Sun, Thermal control of composite sandwich structure with lattice truss cores, J. Thermophys. Heat Transfer 29 (1) (2015) ••••••••••••

[21] X.Q. Zhang, X. Jin, G.N. Xie, H.B. Yan, 2017. Thermo-fluidic comparison between sandwich panels with tetrahedral lattice cores fabricated by casting and metal sheet folding. Energies. 10, 906.

[22] J.H. Joo, B.S. Kang, K.J. Kang, Experimental studies on friction factor and heat transfer characteristics through wire-woven bulk kagome structure, Exp. Heat Transfer, 22 (2) (2009) ••••••••••••

[23] B.B. Shen, H.B. Yan, H.Q. Xue, G.N. Xie, The effects of geometrical topology on fluid flow and thermal performance in Kagome cored sandwich panels, Appl. Therm. Eng. 142 (2018) ••••••••••••

[24] G.M. Yang, C. Hou, M.Y. Zhao, W. Mao, 2019. Comparison of convective heat transfer for Kagome and tetrahedral truss-cored lattice sandwich panels. Sci. Rep. 9, 3731.

[25] X.H. Bai, Z.H. Zheng, A. Nakayama, 2019. Heat transfer performance analysis on lattice core sandwich

panel structures. Int. J. Heat Mass Transfer. 143, 118525.

[26] A. Chaudhari, P. Ekade, S. Krishnan, Experimental investigation of heat transfer and fluid flow in octet-truss lattice geometry, Int. J. Therm. Sci. 143 (2019) • • • • • •••••••

[27] P. Ekade, S. Krishnan, Fluid flow and heat transfer characteristics of octet truss lattice geometry, Int. J. Therm. Sci. 137 (2019) • • • • • • • •••••••••

[28] H.B. Yan, Q.C. Zhang, T.J. Lu, T. Kim, A lightweight X-type metallic lattice in single-phase forced convection, Int. J. Heat Mass Transfer 83 (2015) • • • • • • • •••••••••

[29] H.B. Yan, X.H. Yang, T.J. Lu, G.N. Xie, Convective heat transfer in a lightweight multifunctional sandwich panel with X-type metallic lattice core, Appl. Therm. Eng. 127 (2017) • • • • • • • • •••••••••••

[30] X. Jin, B.B. Shen, H.B. Yan, B. Sunden, G.N. Xie, Comparative evaluation of thermofluidic characteristics of sandwich panels with X-lattice and pyramidal-lattice cores, Int. J. Heat Mass Transfer 127 (2018) • • • • • • • •••••••••

[31] Q.C. Zhang, A.P. Chen, C.Q. Cheng, T.J. Lu, Ultralight X-type lattice sandwich structure (II): micromechanics modeling and finite element analysis, Sci. China Ser. E: Tech. Sci. 52 (9) (2009) • • • • • • • • • •••••••••••

[32] J.N. Sweet, E.P. Roth, M. Moss, Thermal conductivity of Inconel 718 and 304 stainless steel, Int. J. Thermophys. 8 (5) (1987) 593±606.

[33] H.W. Coleman, W.G. Steele, Experimentation, Validation, and Uncertainty Analysis for Engineers, third ed., John Wiley & Sons Inc., Hoboken, 2009.

[34] F.R. Menter, M. Kuntz, R. Langtry, Ten years of industrial experience with the SST turbulence model, in: K. • • • • • • • • Y. Nagano, M. Tummers (Eds.), Turbulence Heat and Mass Transfer, Begell House Inc., Danbury, 2003, pp. • • • • • • • •••••••••

[35] F.R. Menter, Two-equation eddy-viscosity turbulence models for engineering applications, AIAA J. 32 (8) (1994) • • • • • • • • • •••••••••••

[36] J.P. Abraham, E.M. Sparrow, J.C.K. Tong, Heat transfer in all pipe flow regimes: laminar, transitional/intermittent and turbulent, Int. J. Heat Mass Transfer 52 (2009) • • • • • • • •••••••••

[37] J.P. Abraham, E.M. Sparrow, W.J. Minkowycz, Internal-flow Nusselt numbers for the low-Reynolds number end of the laminar-to-turbulent transition regime, Int. J. Heat Mass Transfer 54 (2011) • • • • • • • •••••••••

[38] E.W. Lemmon, M.L. Huber, M.O. McLinden, NIST Standard Reference Database 23: Reference Fluid

Thermodynamic and Transport Properties, version 7.1, 2003.

[39] CFX 14.5, ANSYS CFX-Solver Theory Guide, ANSYS Inc., Canonsburg, 2012.

[40] V. Gnielinski, On heat transfer in tubes, Int. J. Heat Mass Transfer 63 (2013) ••••••••••••••

[41] P.F. Li, J.E. Seem, Y.Y. Li, A new explicit equation for accurate friction factor calculation of smooth pipes, Int. J. Refrig. 34 (2011) ••••••••••••••

[42] C. Hong, T. Nakamura, Y. Asako, I. Ueno, Semi-local friction factor of turbulent gas flow through rectangular microchannels, Int. J. Heat Mass Transfer 98 (2016) ••••••••••••••

[43] V. ••••••Vortex identification: new requirements and limitation, Int. J. Heat Fluid Flow 28 (2007) ••••••••••••••

[44] K. Nagata, Y. Sakai, T. Inaba, H. Suzuki, O. Terashima, H. Suzuki, 2013. Turbulence structure and turbulence kinetic energy transport in multiscale/fractal-generated turbulence. Phys. Fluids. 25, 065102.

[45] A. Cimarelli, A. Leonforte, D. Angeli, On the structure of the self-sustaining cycle in separating and reattaching flows, J. Fluid Mech. 857 (2018) ••••••••••••••

[46] A. Cimarelli, A. Leonforte, E. De Angelis, A. Crivellini, D. Angeli, On negative turbulence production phenomena in the shear layer of separating and reattaching flows, Phys. Lett. A 383 (10) (2019) ••••••••••••••

LIST OF TABLE AND FIGURE CAPTIONS

Table 1. Geometric parameters of the tested X-lattice cored honeycomb.

Parameter	Value	Parameter	Value
b_1	2.70 mm	t_f	1.00 mm
b_2	2.31 mm	t_j	0.91 mm
H_c	9.66 mm	t_s	0.90 mm
l	12.0 mm	w	6.00 mm
L	120 mm	w_j	4.15 mm
r_1	0.30 mm	w_l	2.16 mm
r_2	4.30 mm	W	127 mm
r_3	1.05 mm	••	50°
r_4	1.00 mm	••	42°

Table 2. Operating conditions of the present pressure drop and heat transfer measurements.

Parameter	Value
Reynolds number, Re_H	••••••••••••••••••
Inlet air temperature, T_{in}	23.9•32.4 ëC
Applied heat flux, q©	••••••••••••W/m²•••

Table 3. Thermo-physical properties of air used in the numerical simulations.

Reynolds number	Density ••[kg/m³]	Dynamic viscosity ••×10⁵ [Pa´s]	Thermal conductivity k_f [W/(mK)]
3591	1.0888	1.8979	0.02679
4727	1.0947	1.8946	0.02674
5287	1.0834	1.9144	0.02703
5886	1.0857	1.9148	0.02704
6539	1.0866	1.9177	0.02708
7450	1.0875	1.9234	0.02716

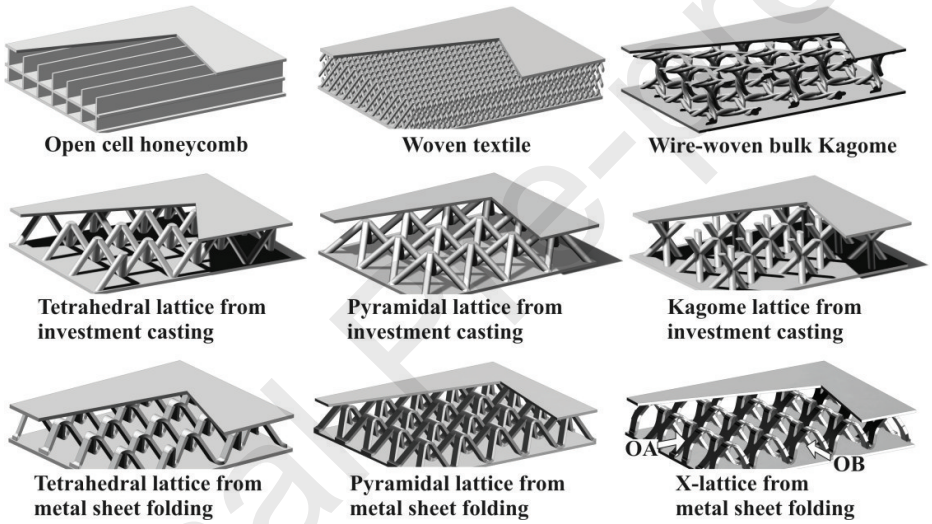

Fig. 1. Schematic illustration of periodic cellular materials with a variety of topologies.

(a) (b)

Fig. 2. Proposal of a new periodic cellular material based on thermo-fluidic mechanisms: (a) the unique flow induced by the X-lattice in a sandwich panel [28]; (b) details of the newly invented X-lattice cored honeycomb.

(a) (b)

Fig. 3. Details of the test sample: (a) an overview; (b) geometric parameters governing the morphology.

(a)

(b)

Fig. 4. Test facilities: (a) three-dimensional illustration of the wind tunnel system and the instruments; (b) details of the heating and temperature measurement assembly.

(a)

(b)

Fig. 5. Numerical models: (a) computational domain and boundary conditions; (b) representative meshes.

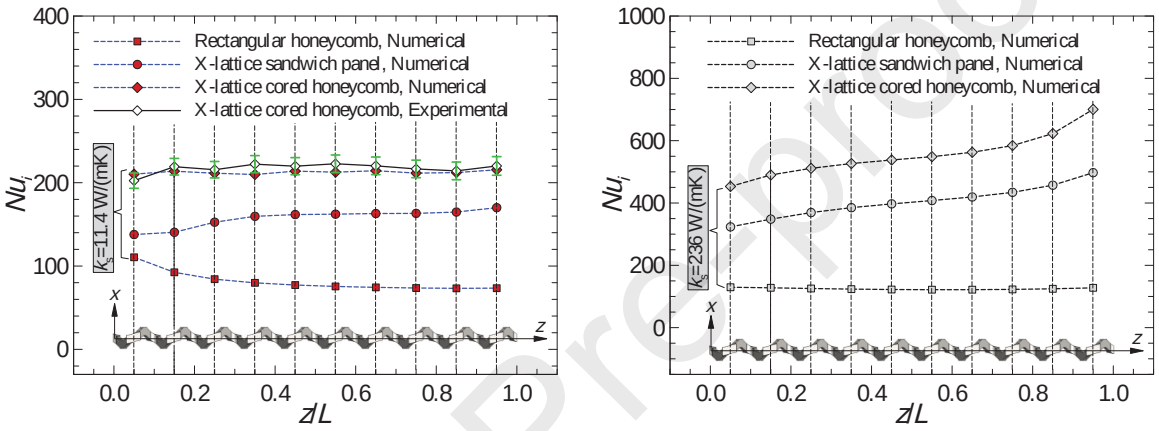

Fig. 6. Streamwise profile of Nusselt number at Re_H = 7450: (a) k_s = 11.4 W/(mK); (b) k_s = 236 W/(mK).

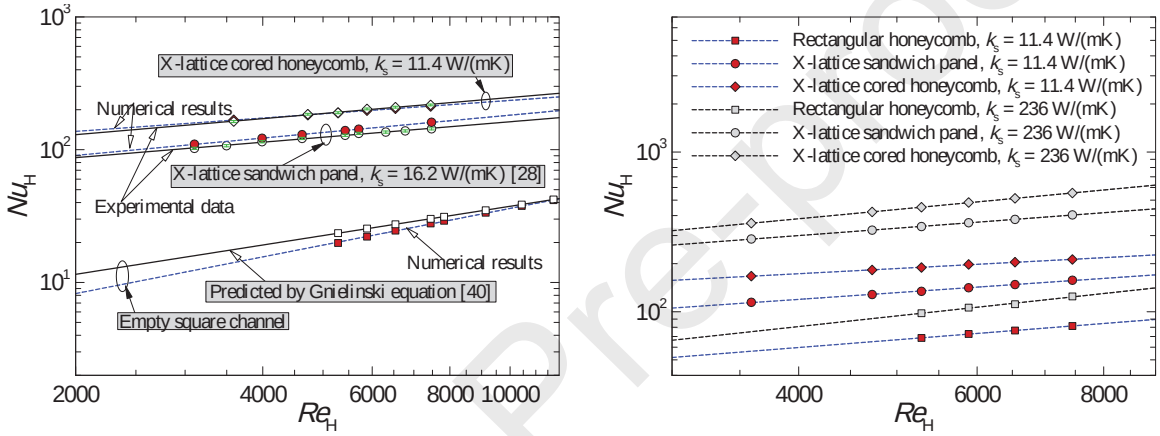

Fig. 7. Comparison of overall heat transfer under the fixed Reynolds number condition: (a) validation of the numerical model by comparison between experimental/empirical and numerical results; (b) overall Nusselt number as a function of Reynolds number for the three PCMs.

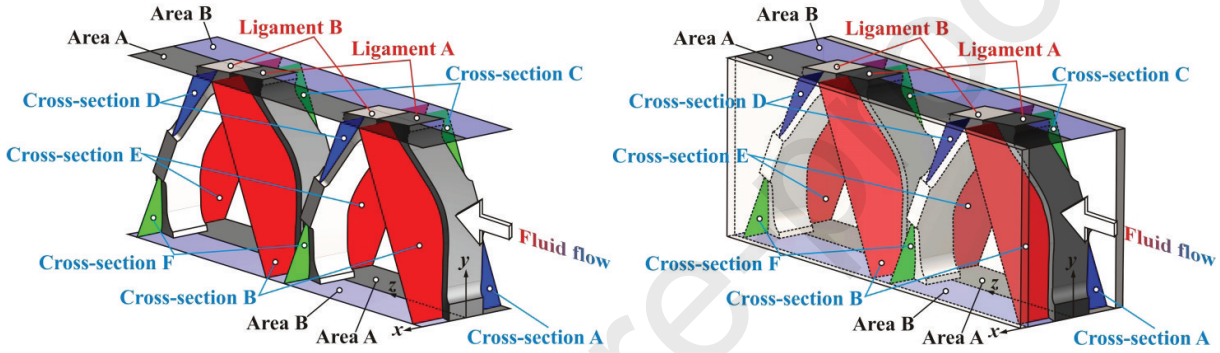

Fig. 8. Classification of the representative lattice ligaments, cross-sections and the endwall for the convenience of interpreting fluid flow and local heat transfer mechanisms: (a) the X-lattice sandwich panel; (b) the X-lattice cored honeycomb.

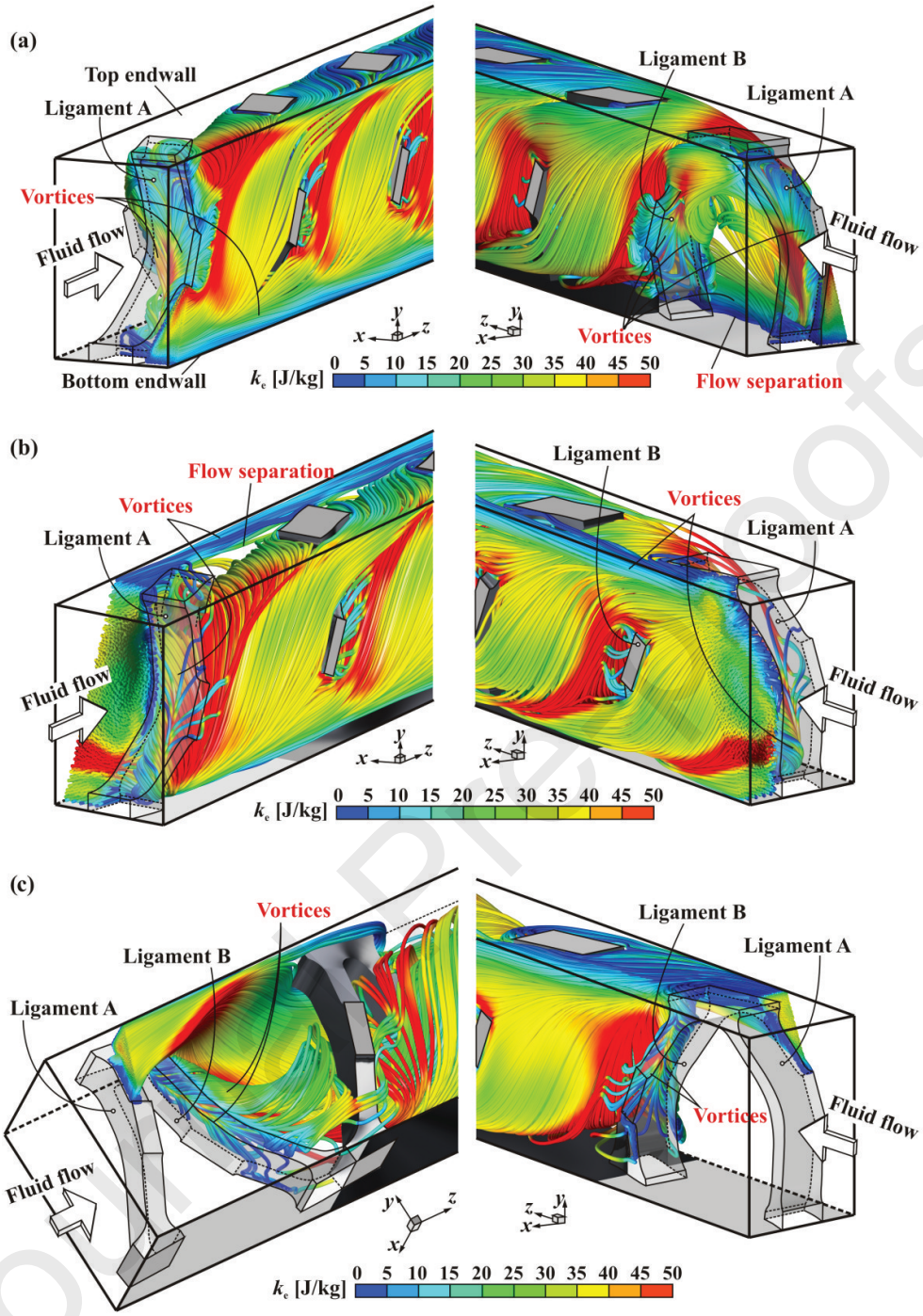

Fig. 9. Fluid flow in the X-lattice sandwich panel characterized by three-dimensional streamlines at a representative Reynolds number of Re_H = 7450, separately released from (a) cross-section A, (b) cross-section B as well as (c) cross-section C as schematically shown in Fig. 8. The streamlines are coloured by the turbulent kinetic energy magnitude.

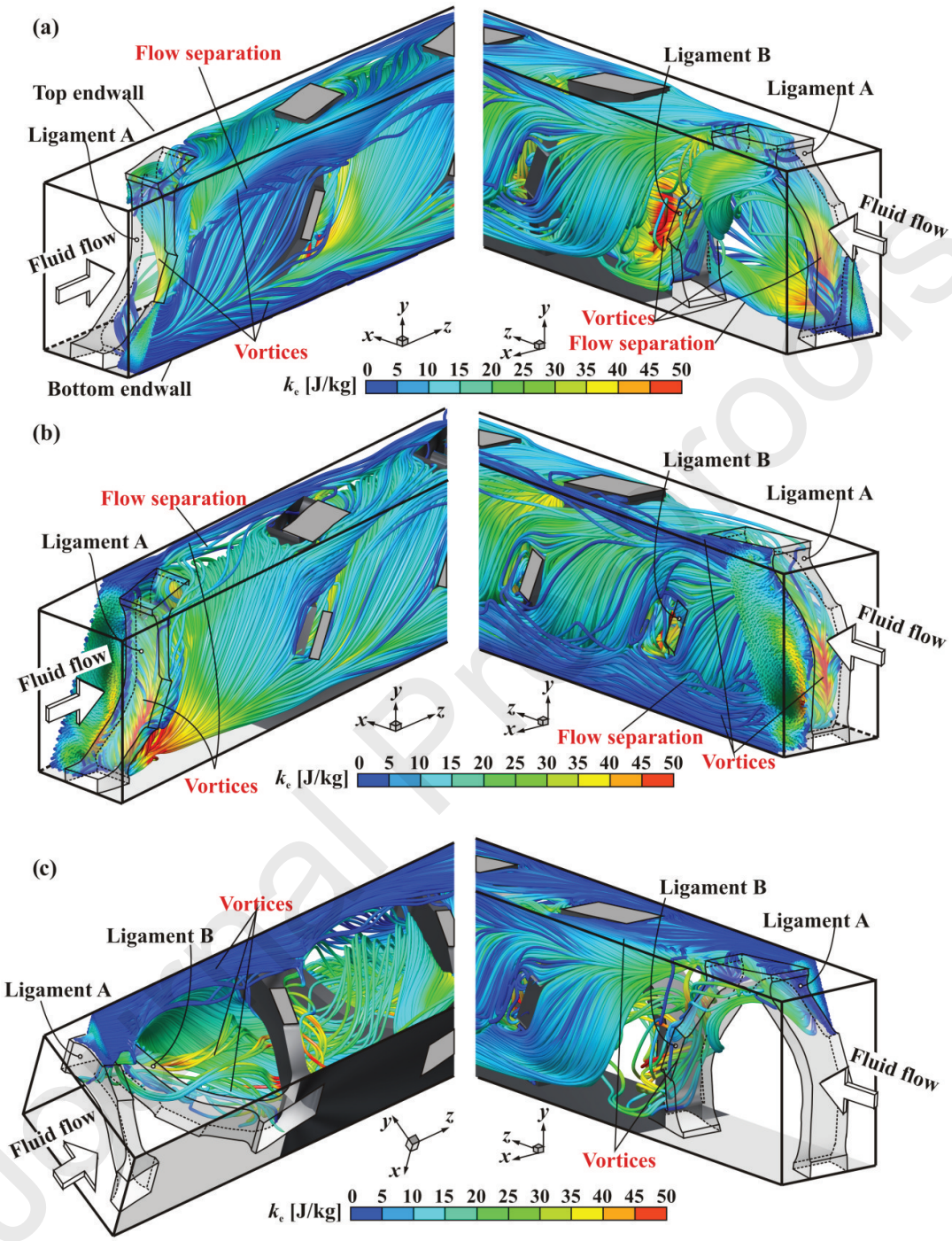

Fig. 10. Fluid flow in the X-lattice cored honeycomb characterized by three-dimensional streamlines at a representative Reynolds number of Re_H = 7450, separately released from (a) cross-section A, (b) cross-section B and (c) cross-section C as shown in Fig. 8. The streamlines are coloured by the turbulent kinetic energy magnitude.

Fig. 11. Fluid flow in the X-lattice cored honeycomb characterized by three-dimensional streamlines at a representative Reynolds number of Re_H = 7450, separately released from (a) cross-section D, (b) cross-section E and (c) cross-section F as shown in Fig. 8. The streamlines are coloured by the turbulent kinetic energy magnitude.

(a)

(b)

Fig. 12. Vortex structures visualized by the iso-surfaces of the positive second invariant of the velocity gradient tensor according to the *Q*-criterion [43] at Re_t = 7450: (a) the X-lattice sandwich panel; (b) the X-lattice cored honeycomb. The iso-surfaces are coloured by the turbulent kinetic energy magnitude.

(a)

(b)

Fig. 13. Pressure distributions in five representative planes placed at the inlet, middle and the exit of the sixth and the seventh unit cells at Re_H = 7450, where p and p_{min} are separately the local pressure and the minimum pressure on each plane: (a) the X-lattice sandwich panel; (b) the X-lattice cored honeycomb.

Fig. 14. Surface streamlines and distributions of the tangential velocity magnitude (V_t) in several representative planes at Re_H = 7450: (a) the X-lattice sandwich panel; (b) the X-lattice cored honeycomb.

Fig. 15. Distributions of the velocity magnitude (V_m) in several representative planes at Re_H = 7450: (a) the rectangular honeycomb; (b) the X-lattice sandwich panel; (c) the X-lattice cored honeycomb.

Fig. 16. Distributions of the velocity magnitude (V_m) in several representative planes at Re_H = 7450: (a) the rectangular honeycomb; (b) the X-lattice sandwich panel; (c) the X-lattice cored honeycomb.

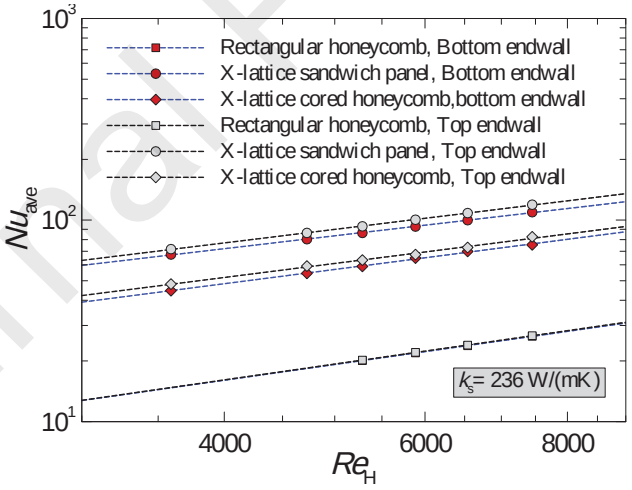

(d)

Fig. 17. Comparison of local heat transfer on the endwall: •••••local heat transfer distribution at Re_H = 7450 for the rectangular honeycomb, the X-lattice sandwich panel and the X-lattice cored honeycomb, respectively; (d) area-averaged Nusselt number as a function of Reynolds number.

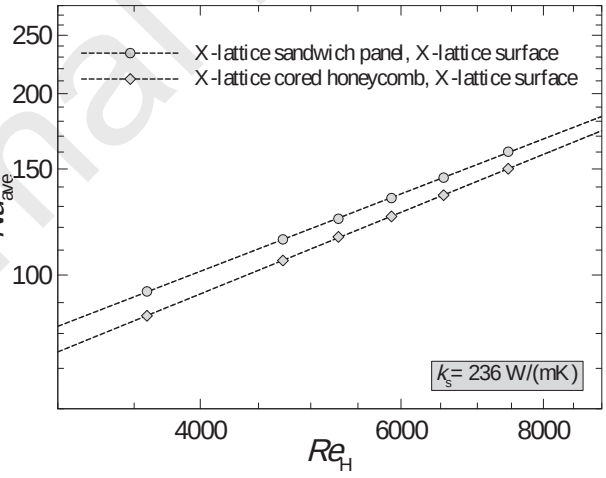

(c)

Fig. 18. Comparison of local heat transfer on the X-lattice surface: (a) local heat transfer distribution at Re_H = 7450; (b) area-averaged Nusselt number as a function of Reynolds number.

(a)

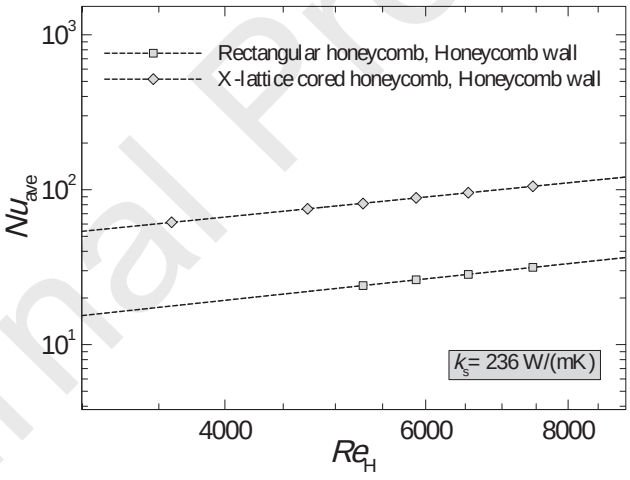

(b)

Fig. 19. Comparison of local heat transfer on the honeycomb wall: (a) local heat transfer distribution at Re_H = 7450; (b) area-averaged Nusselt number as a function of Reynolds number.

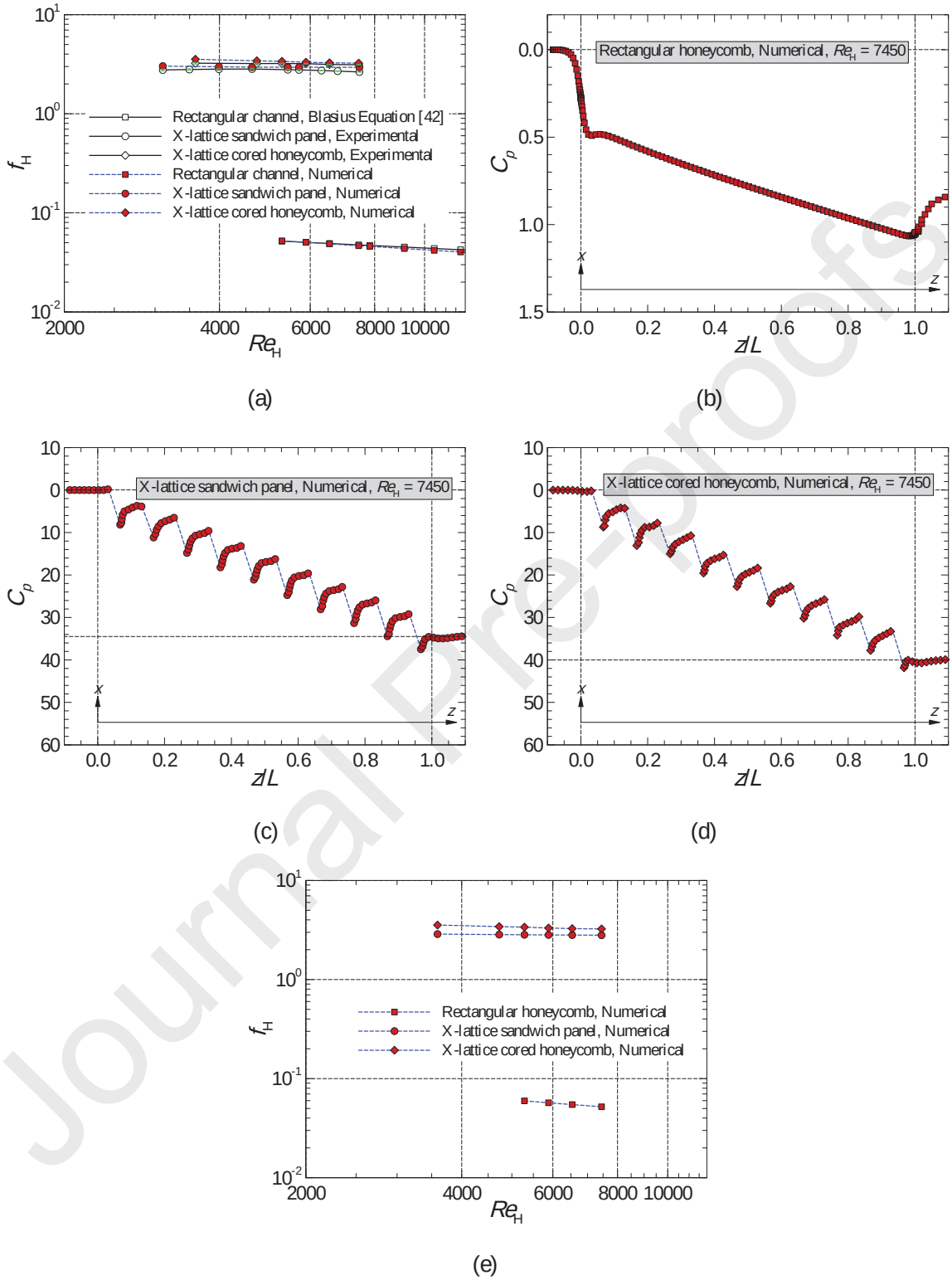

Fig. 20. Comparison of pressure drop: (a) validation of the numerical model; (b•••) streamwise profiles of static pressure; (d) friction factor as a function of Reynolds number finally used for comparison.

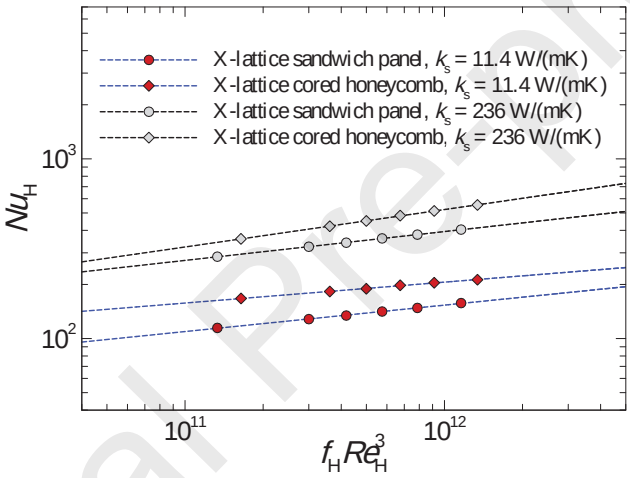

Fig. 21. Comparison of overall thermal performance under the fixed pumping power condition.

Highlights

- A new cellular metal by integrating the X-lattice with honeycomb is proposed.
- This new cellular material exhibits better heat transfer than references ones.
- The honeycomb wall significantly modifies the vortex flows and turbulence field.
- The honeycomb wall deteriorates heat transfer on the endwall and lattice ligaments.
- The X-lattice significantly enhances local heat transfer on the honeycomb walls.

Conflict of interest statement

We declare that we have no financial and personal relationships with other people or organizations that can inappropriately influence our work; there is no professional or other personal interest of any nature or kind in any product, service or company that could be construed as influencing the position presented in, or the review of this manuscript.

We confirm that the manuscript has been read and approved by all named authors. No other persons who satisfied the criteria for authorship but are not listed. We further confirm that no opposition is given with the order of authors listed in the manuscript from any of us.

We confirm that we have given due consideration to the protection of intellectual property associated with this work. No impediment exists to publication with respect to intellectual property. We declare that we have followed the regulations of our institutions concerning intellectual property.

We understand that the Corresponding Author is the sole contact for the Editorial process, who is responsible for communication with the other authors about progress, submissions of revisions and final approval of proofs. A current, correct email address has been provided which is accessible by the Corresponding Author and which has been configured to accept email from tjlu@nuaa.edu.cn.

Signed by all authors as follows:

Hongbin Yan _____

Qiancheng Zhang _____

Weijian Chen _____

Gongnan Xie _____

Jianjun Dang _____

Tianjian Lu _____